minerals

MDPI

Article

Loveringite from the Khamal Layered Mafic Intrusion: The First Occurrence in the Arabian Shield, Northwest Saudi Arabia

Bassam A. Abuamarah [1], Fahad Alshehri [1,*], Mokhles K. Azer [2] and Paul D. Asimow [3]

[1] Geology and Geophysics Department, College of Science, King Saud University, Riyadh 11451, Saudi Arabia
[2] Geological Sciences Department, National Research Centre, Dokki, Cairo 12622, Egypt
[3] Division of Geological & Planetary Sciences, California Institute of Technology, Pasadena, CA 91125, USA
* Correspondence: falshehria@ksu.edu.sa; Tel.: +966-11-4677053

Abstract: Loveringite, a rare member of the crichtonite group with nominal formula (Ca,Ce)(Ti,Fe,Cr,Mg)$_{21}$O$_{38}$, was found in the Khamal layered mafic intrusion, the first known locality for this mineral in the Arabian Shield. The Khamal intrusion, a large post-collisional mafic complex, is lithologically zoned, bottom to top, from olivine gabbro through gabbronorite, hornblende gabbro, anorthosite, and diorite to quartz diorite. Loveringite is found near the base of the complex, as an intercumulus phase in olivine gabbro. Most loveringite grains are homogeneous, although a few grains are zoned from cores rich in TiO_2, Al_2O_3, Cr_2O_3, and CaO towards rims rich in FeO*, ZrO_2, V_2O_3, Y_2O_3, and rare earth elements (REE). Petrographic relations indicate that loveringite formed after crystallization of cumulus olivine, pyroxenes, and plagioclase. Anhedral and corroded crystals of loveringite are surrounded by reaction rims of Mn-bearing ilmenite and baddeleyite, suggesting that the residual liquid evolved into and subsequently out of the stability field of loveringite. The budget of incompatible elements (Zr, Hf, REE, U, and Th) hosted in loveringite is anomalous for a primitive mafic liquid. Saturation in loveringite is likely the result of early contamination of the primary melt by anatexis of country rock, followed by isolation of evolving liquid in intercumulus space that restricted communication with the overlying magma chamber. The zoned crystals likely reflect diffusive equilibration between residual loveringite grains and their reaction rims of ilmenite.

Keywords: Arabian Shield; layered mafic intrusion; Khamal intrusion; olivine gabbro; loveringite

Citation: Abuamarah, B.A.; Alshehri, F.; Azer, M.K.; Asimow, P.D. Loveringite from the Khamal Layered Mafic Intrusion: The First Occurrence in the Arabian Shield, Northwest Saudi Arabia. *Minerals* **2023**, *13*, 172. https://doi.org/10.3390/min13020172

Academic Editor: Jim Lee

Received: 16 December 2022
Revised: 16 January 2023
Accepted: 19 January 2023
Published: 25 January 2023

1. Introduction

Loveringite is a rare accessory mineral from the crichtonite group with the nominal chemical formula (Ca,Ce)(Ti,Fe,Cr,Mg)$_{21}$O$_{38}$. It was discovered in the Jimberlana layered intrusion of Western Australia [1,2]. Igneous loveringite has since been reported in a number of layered mafic intrusions [3–9], ophiolites [10], mantle xenoliths [11], and kimberlites [12]. Loveringite is an efficient "collector" of incompatible elements (REE, Y, U, Th, Zr, and Hf) that accumulate in residual liquids during magmatic differentiation, reaching saturation at an advanced stage of local crystallization, though it may be found in the most primitive lithologies at the base of many intrusions. It serves as a petrogenetic indicator of the late evolution of intercumulus liquids and a tracer of the concentrations of economically significant elements (REE, Y, U, Th, Zr, and Hf) in its host intrusions [1,13].

In this paper we report the first occurrence of loveringite in the Neoproterozoic Arabian Shield, from the Khamal layered intrusion of western Saudi Arabia. The Khamal intrusion hosts ore deposits characteristic of layered intrusions, including Fe-Ti-apatite-rich nelsonite and Fe-Ti oxides [14,15]. We present the textural and mineral chemical description of the loveringite and associated minerals in the olivine gabbro of the Khamal intrusion, and briefly consider the implications of this occurrence.

2. Brief Geological Description

The Arabian Shield features several Neoproterozoic post-collisional layered mafic intrusions [16]. The Khamal intrusion is a well-known example [14,15]. It is situated in the northwestern part of the Arabian Shield, close to the Yanbu suture zone that separates the Midyan Terrane from the Hijaz terrane (Figure 1). The intrusion has an elliptical planform, 13 km from north to south and 6 km from east to west. It forms a broad, 200 m high dome-shaped peak surrounded by wadis. According to a Sm-Nd mineral isochron, it was formed at 618 ± 27 Ma [17]. It intruded into ophiolitic rocks, a volcano-sedimentary sequence of island-arc affinity, and a syntectonic granodiorite; it is intruded in turn by post-collisional alkaline granite (Figure 2). The intrusive relations are supported by local, narrow contact-metamorphic zones of hornfels in country rocks around the margins of the intrusion, by a fine-grained quenched zone at the margin of the intrusive rocks, by xenoliths of country rock in the intrusion, and by offshoots of gabbro penetrating the metamorphic halo. In the southern part of the mapped area, intrusion of later alkaline granite is marked by deuteric alteration and formation of highly altered rock (uralitized gabbro).

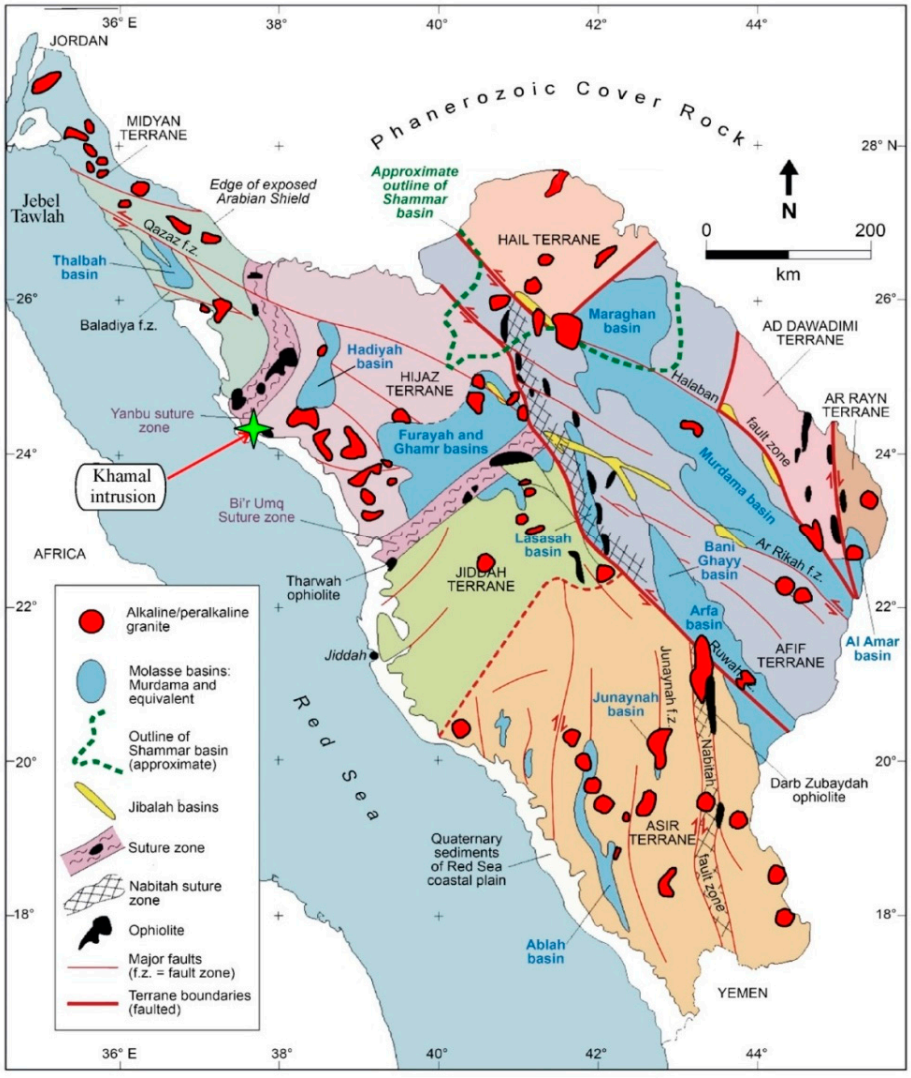

Figure 1. Simplified geologic map of the Arabian Shield in Saudi Arabia (modified after [18]). The location of the Khamal intrusion is indicated by a green asterisk.

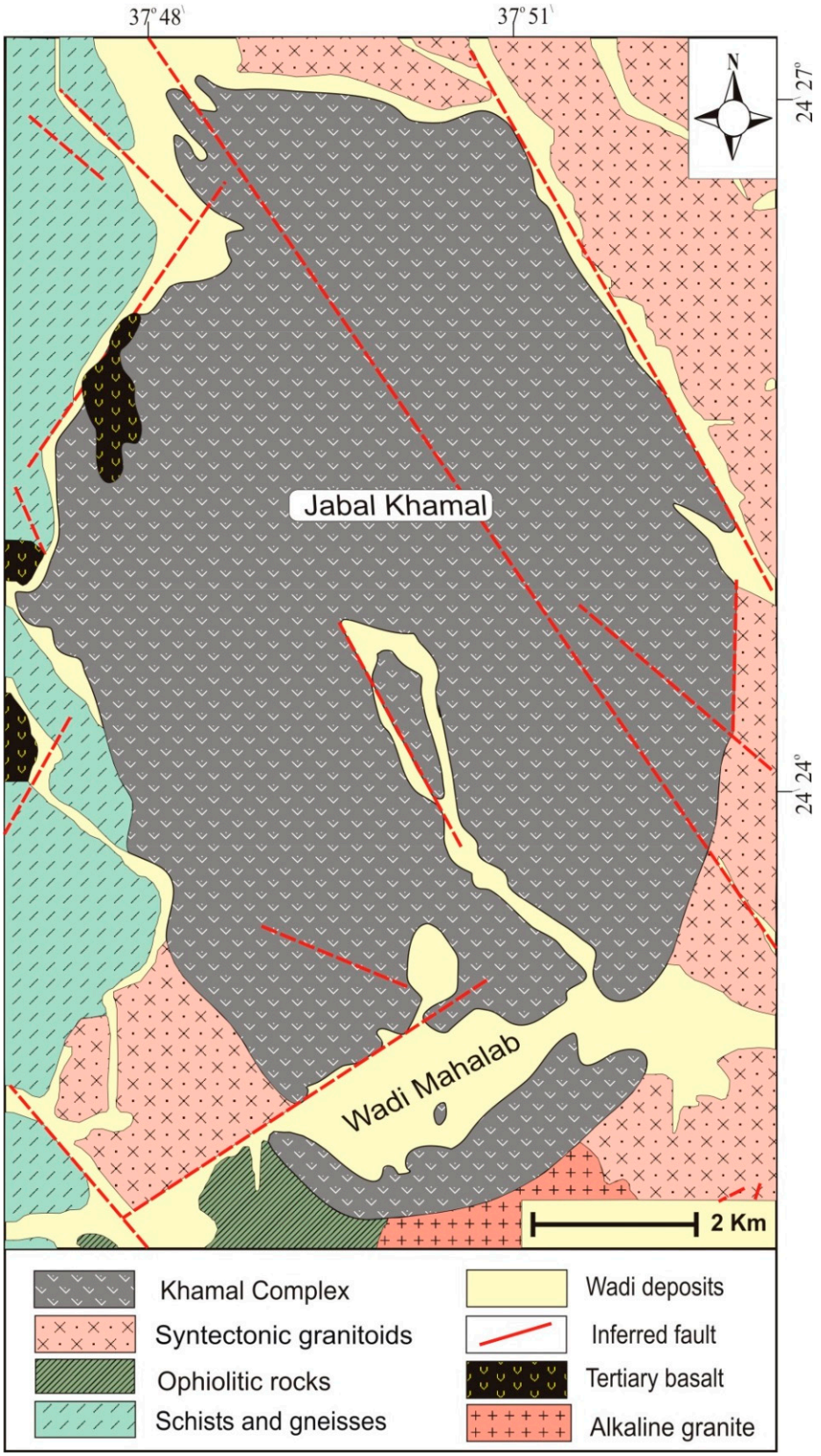

Figure 2. Geologic map of Wadi Khamal area (modified after [14]).

3. Petrography

Based on the microscopic studies, the principal lithologies of the Khamal intrusion are distinguished into olivine gabbro, gabbronorite, hornblende gabbro, anorthosite, diorite, and quartz diorite. The petrographic descriptions of most rock types below are deliberately brief, but olivine gabbro is described in more detail because it hosts the loveringite.

Gabbronorite is fine- to medium-grained and consists of plagioclase and clinopyroxene with subordinate orthopyroxene and amphibole (hornblende). Opaques, apatite, zircon, and green spinel are the main accessory minerals. Some gabbronorite outcrops feature sparse bands rich in apatite (up to 8 volume %) and Fe-Ti oxides (up to 15%). Hornblende gabbro is medium- to coarse-grained and consists mostly of plagioclase, clinopyroxene, and amphibole with minor interstitial orthopyroxene and biotite. The main accessory minerals are opaques, apatite, and zircon. Anorthosite is medium- to coarse-grained with local bands of very coarse plagioclase pegmatite. Plagioclase is the essential mineral with minor olivine, amphibole, and clinopyroxene. Accessory minerals include Fe-Ti oxides, apatite, and zircon. Dioritic rocks are medium-grained and have hypidiomorphic granular texture. They include diorite (<5% quartz) and quartz-diorite (5%–10% quartz). Plagioclase and mafic minerals are dominant in both rock types, with sparse crystals of quartz and K-feldspars. The main accessory minerals in the diorites include opaques, apatite, titanite, and zircon.

Olivine gabbro is a medium- to coarse-grained melanocratic rock showing subophitic texture and consisting essentially of plagioclase, clinopyroxene, and olivine (5%–10%) with minor amounts of orthopyroxene (<5%) and amphibole (<2%). The accessory minerals include Fe-Ti oxides, apatite, zircon, green spinel, loveringite, and baddeleyite. Plagioclase (50–60 modal %) is the essential mineral and occurs as subhedral to euhedral tabular crystals that are locally zoned and include small, rounded crystals of olivine (Figure 3a). The entrapment of olivine in plagioclase indicates that the onset of olivine crystallization occurred before the end of plagioclase crystallization. Clinopyroxene (15–22 modal %) occurs as subhedral to anhedral crystals that may display simple twins. Along the cleavage planes and cracks, it is partly altered to amphibole and chlorite. Orthopyroxene (<5 modal %) forms subhedral to anhedral equant to elongate individual crystals and rims around olivine. A few small inclusions and exsolution lamellae of clinopyroxene are observed in orthopyroxene. Some plagioclase crystals are enclosed in the orthopyroxene and clinopyroxene forming poikilitic texture. Olivine (5–12 modal %) occurs as anhedral rounded crystals that show alteration along rims or fractures into sepiolite and chlorite. Some olivine crystals are surrounded by clinopyroxene and amphibole, forming corona texture (Figure 3b).

Loveringite, the target of the present work, was identified in two samples (KG7 and KG12) of olivine gabbro. It mostly occurs as anhedral crystals, corroded and surrounded by reaction rims of Mn-bearing ilmenite (Figure 3c), apatite, and baddeleyite (Figure 3d). However, rare euhedral crystals of loveringite are observed in some sections. There are also rare instances where loveringite is surrounded by assemblages of secondary minerals such as amphibole and chlorite (Figure 3e). In a few cases, loveringite includes apatite or fine, elongated segregations of baddeleyite, apparently oriented along crystallographic planes of the host loveringite. In reflected light, loveringite is distinguished by its pinkish hue, but the distinctive ilmenite rims around most loveringite grains are the easiest way to find the loveringite in both the optical and electron microscope.

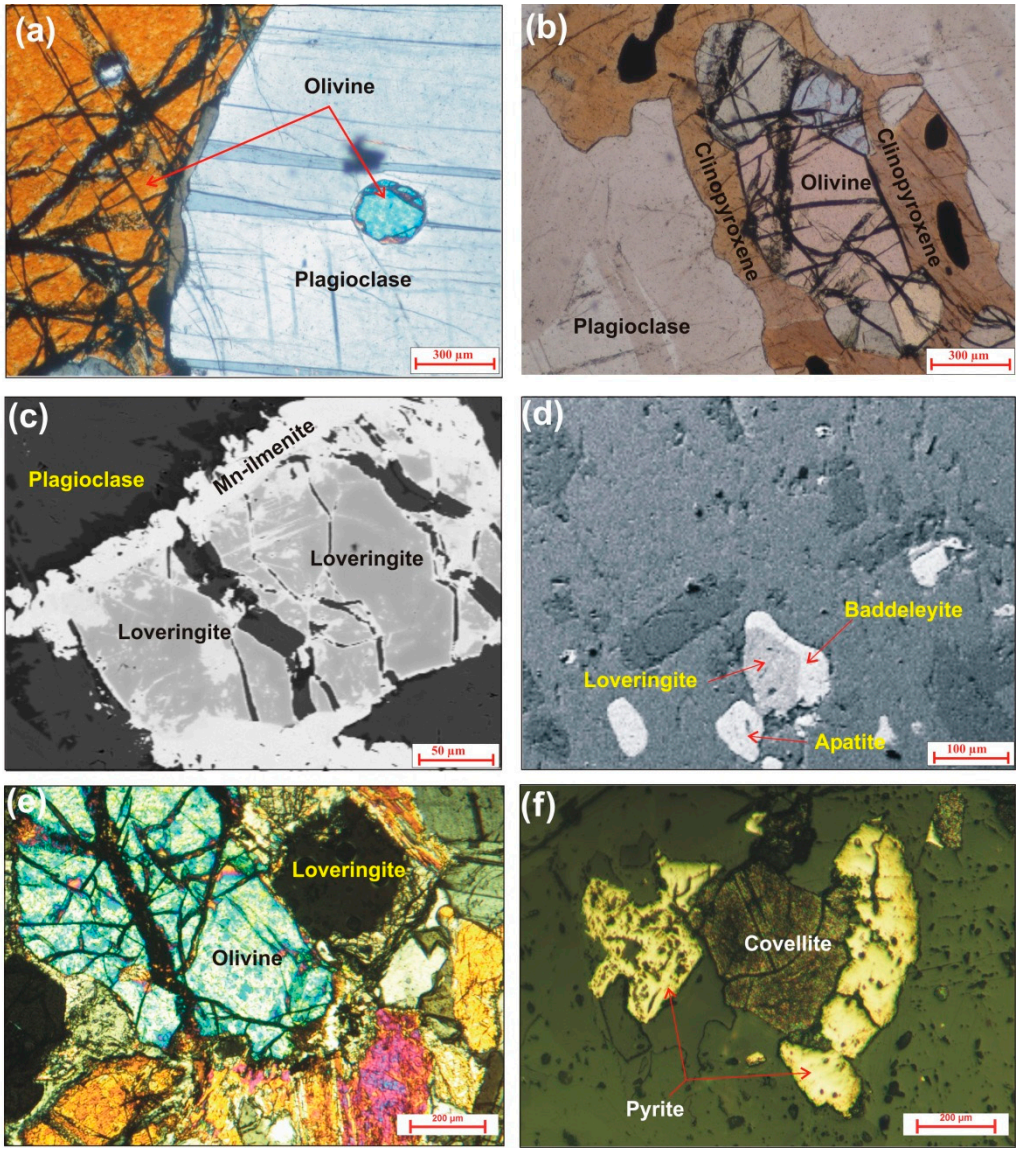

Figure 3. Photomicrographs showing textures and mineral characteristics of olivine gabbro: (**a**) plagioclase containing small, rounded crystals of olivine in cross-polarized transmitted light, (**b**) olivine surrounded by pyroxene forming corona texture in plane-polarized transmitted light, (**c**) backscattered electron image showing loveringite crystal rimmed by ilmenite, (**d**) backscatter image showing apatite and baddeleyite crystals around loveringite, (**e**) secondary minerals such as amphibole and chlorite surrounding loveringite in cross-polarized light, and (**f**) sulfide minerals in reflected light.

Apatite occurs as small subhedral to euhedral crystals that are usually located in the interstices or near the grain boundaries of early magmatic silicates, associated with ilmenite and loveringite. Apatite is also found as euhedral inclusions in plagioclase and rarely as anhedral inclusions in loveringite. Ilmenite occurs as rims around or along cracks in loveringite. Continuous ilmenite rims are observed around most corroded loveringite grains. Green spinel occurs as disseminated anhedral to subhedral fine crystals and as clusters of rounded crystals. Texturally, green spinel seems to have appeared late in the crystallization sequence. Baddeleyite occurs as disseminated fine crystals and in rims around loveringite. Some samples of olivine gabbro contain sulfide minerals; reflected light microscopy shows that the primary sulfides are pyrite and chalcopyrite, replaced by covellite and goethite (Figure 3f).

4. Mineral Chemistry

The composition of the essential minerals in the loveringite-bearing olivine gabbro samples (KG7 and KG12) were analyzed using a CAMECA SX-100 electron probe microanalysis (EPMA) at the University of Vienna, Department of Lithospheric Research, Austria. The operating conditions were 15 kV accelerating voltage, 20 nA probe current, a focused (1 µm diameter) beam, and 10 s count time on peak. The analyses were made against natural and synthetic mineral standards. The correction of the raw data was conducted using an online ZAF program. The analyzed minerals include olivine, pyroxenes, plagioclase, ilmenite, green spinel, loveringite, and baddeleyite. The complete set of electron microprobe analyses (in wt.%) and suitable structural formulae of these minerals are given in Tables 1–6.

4.1. Olivine (Table 1)

Forsterite contents (79.0–85.2 mol %) and NiO contents (0.11–0.26 wt.%, average 0.18) of olivine are similar to olivine from layered intrusions of the Arabian-Nubian Shield (ANS) [19–22] but are lower than olivine in ANS ophiolites [23–26] or the mantle olivine array [27] (Figure 4a). MnO (0.17–0.33 wt. %) and CaO (<0.04 wt. %) contents are typical of olivine from layered intrusions as well.

4.2. Pyroxenes (Table 2)

Pyroxene analyses in olivine gabbro include both orthopyroxene and clinopyroxene. According to the conventional nomenclature [28], the orthopyroxene is classified as enstatite, whereas the clinopyroxene is classified as diopside. Enstatite has a range of Mg# [100 × Mg/(Mg + Fe^{2+}) on a molar basis] from 83 to 88 (average 85.5). Diopside is more magnesian, with Mg# from 87 to 96 (average 91.4), and highly calcic (47–49 mol % Wo component).

4.3. Plagioclase (Table 3)

The analyzed plagioclase crystals are homogenous within individual specimens. They have high CaO contents (15.46–18.76 wt. %) and low Na_2O (1.43–2.64 wt.%) and K_2O (<0.02 wt.%). They are calcic in composition and are classified as bytownite ($An_{74.8}$ to $An_{85.8}$).

4.4. Ilmenite (Table 4)

Ilmenite rims around loveringite are composed mainly of TiO_2 (46.8–50.6 wt.%) and FeO* (that is, total Fe expressed as FeO, 44.2–50.6 wt.%), with significant MnO (2.6–4.0 wt.%). End-member components of the ilmenite solid solution, calculated according to [29], include 78.9 to 87.5 mol% (average 84.1) ilmenite component, 3.5 to 14.1 mol% (average 8.0) hematite component, and 5.6 to 8.5 mol% (average 6.8) pyrophanite ($MnTiO_3$) component. These hematite and pyrophanite contents indicate relatively oxidizing magmatic conditions [30–32]; textures do not indicate equilibrium with coexisting spinel solid solutions, so we have not attempted quantitative oxybarometry.

4.5. Green Spinel (Table 5)

Major oxides of the analyzed green spinels are Al_2O_3 (53.9–58.1 wt.%), FeO* (26.2–32.0 wt.%), and MgO (10.6–14.6 wt.%). Other major oxides are very minor or below the detection limits. In terms of the end members of spinel solid solutions, these analyses are dominated by spinel *sensu stricto* and hercynite, with at most 10 mol% magnetite component and <2 mol% of others. Mg# ranges from 43 to 59 with an average of 53. Green spinel is a characteristic accessory mineral in mafic layered intrusion in the ANS [19].

Table 1. Microprobe analyses of olivine in the olivine gabbro of the Khamal mafic intrusion.

Sample No.	**KG7**										**KG12**									
Spot No.	**Ol#1**	**Ol#2**	**Ol#3**	**Ol#4**	**Ol#5**	**Ol#6**	**Ol#7**	**Ol#8**	**Ol#9**	**Ol#10**	**Ol#1**	**Ol#2**	**Ol#3**	**Ol#4**	**Ol#5**	**Ol#6**	**Ol#17**	**Ol#8**	**Ol#9**	**Ol#10**
SiO_2	39.24	39.34	40.31	39.82	39.60	40.33	39.83	39.74	39.87	38.98	39.62	39.12	39.37	40.27	39.71	39.50	39.46	38.95	39.33	39.39
TiO_2	<0.01	<0.01	0.01	<0.01	0.01	<0.01	0.01	0.01	<0.01	0.03	0.01	0.01	0.01	0.01	0.01	0.01	<0.01	<0.01	<0.01	0.01
Al_2O_3	<0.01	<0.01	<0.01	<0.01	0.03	<0.01	<0.01	0.01	0.07	0.20	0.04	<0.01	0.01	<0.01	0.04	<0.01	<0.01	<0.01	<0.01	0.02
Cr_2O_3	0.01	0.01	<0.01	<0.01	0.04	<0.01	<0.01	<0.01	0.02	<0.01	0.01	0.04	<0.01	<0.01	<0.01	0.01	<0.01	<0.01	0.03	0.01
FeO	14.03	17.15	17.50	14.48	15.87	14.32	14.34	15.31	15.71	16.74	18.07	14.73	17.79	17.37	19.26	17.10	16.46	18.12	13.41	17.52
MnO	0.21	0.20	0.28	0.18	0.26	0.17	0.22	0.18	0.23	0.33	0.27	0.20	0.27	0.29	0.32	0.27	0.28	0.27	0.22	0.28
MgO	46.06	43.04	43.19	45.86	44.47	46.02	45.47	44.11	44.18	43.24	42.45	45.87	42.69	41.53	41.28	43.58	44.10	42.38	46.54	42.87
CaO	0.01	0.02	0.01	<0.01	0.02	0.01	0.02	0.01	0.02	0.04	0.04	0.01	0.02	0.01	0.14	0.01	0.01	0.02	0.01	0.03
Na_2O	<0.01	<0.01	<0.01	<0.01	0.01	<0.01	<0.01	0.04	0.01	0.01	0.01	0.01	<0.01	<0.01	<0.01	<0.01	<0.01	0.01	<0.01	<0.01
K_2O	<0.01	<0.01	<0.01	<0.01	0.01	<0.01	<0.01	<0.01	<0.01	0.01	<0.01	0.01	<0.01	<0.01	<0.01	<0.01	<0.01	<0.01	<0.01	<0.01
NiO	0.25	0.15	0.14	0.25	0.18	0.26	0.19	0.25	0.18	0.12	0.14	0.20	0.14	0.11	0.13	0.14	0.15	0.14	0.26	0.15
Total	99.81	99.93	101.4	100.6	100.5	101.1	100.1	99.66	100.3	99.70	100.7	100.2	100.3	99.59	100.9	100.6	100.5	99.90	99.79	100.3
Structural formulae on the basis of 4 (O)																				
Si	0.985	0.999	1.008	0.993	0.995	0.998	0.997	1.003	1.002	0.992	1.003	0.982	0.999	1.024	1.008	0.996	0.994	0.995	0.497	0.999
Ti	0.000	0.000	0.000	0.000	0.000	0.000	0.000	0.000	0.000	0.001	0.000	0.000	0.000	0.000	0.000	0.000	0.000	0.000	0.000	0.000
Al	0.000	0.000	0.000	0.000	0.001	0.000	0.000	0.000	0.002	0.006	0.001	0.000	0.000	0.000	0.001	0.000	0.000	0.000	0.000	0.001
Cr	0.000	0.000	0.000	0.000	0.001	0.000	0.000	0.000	0.000	0.000	0.000	0.001	0.000	0.000	0.000	0.000	0.000	0.000	0.000	0.000
Fe(ii)	0.295	0.364	0.366	0.302	0.333	0.296	0.300	0.323	0.330	0.356	0.382	0.309	0.377	0.369	0.409	0.361	0.347	0.387	0.347	0.372
Mn	0.005	0.004	0.006	0.004	0.005	0.004	0.005	0.004	0.005	0.007	0.006	0.004	0.006	0.006	0.007	0.006	0.006	0.006	0.006	0.006
Mg	1.724	1.630	1.610	1.704	1.665	1.698	1.697	1.660	1.654	1.640	1.602	1.717	1.615	1.574	1.563	1.638	1.656	1.614	1.656	1.620
Ni	0.005	0.003	0.003	0.005	0.004	0.005	0.004	0.005	0.004	0.003	0.003	0.004	0.003	0.002	0.003	0.003	0.003	0.003	0.003	0.003
Ca	0.000	0.001	0.000	0.000	0.000	0.000	0.000	0.000	0.000	0.001	0.001	0.000	0.001	0.000	0.004	0.000	0.000	0.001	0.000	0.001
Endmembers (mol %)																				
Fo	85.22	81.56	81.24	84.80	83.09	84.98	84.77	83.54	83.17	81.87	80.48	84.56	80.82	80.74	78.98	81.73	82.45	80.42	82.45	81.11
Fa	14.56	18.22	18.46	15.02	16.64	14.84	14.99	16.26	16.58	17.77	19.22	15.23	18.89	18.94	20.67	17.99	17.26	19.29	17.26	18.60
Tp	0.22	0.22	0.29	0.19	0.27	0.18	0.23	0.20	0.25	0.36	0.30	0.21	0.29	0.32	0.35	0.28	0.29	0.30	0.29	0.30

Table 2. Microprobe analyses of clinopyroxene and orthopyroxene in the olivine gabbro of the Khamal mafic intrusion.

Mineral	**Clinopyroxene**														**Orthopyroxene**							
Sample No.	**KG7**							**KG12**							**KG7**				**KG12**			
Spot No.	**Cpx1**	**Cpx2**	**Cpx3**	**Cpx4**	**Cpx5**	**Cpx6**	**Cpx7**	**Cpx1**	**Cpx2**	**Cpx3**	**Cpx4**	**Cpx5**	**Cpx6**	**Cpx7**	**Opx1**	**Opx2**	**Opx3**	**Opx4**	**Opx1**	**Opx2**	**Opx3**	**Opx4**
SiO_2	52.20	52.21	51.34	52.09	52.05	51.62	51.86	51.72	51.85	51.90	51.79	51.82	52.25	51.56	55.33	55.57	55.42	54.74	54.68	54.76	56.14	54.54
TiO_2	0.42	0.41	0.47	0.40	0.35	0.37	0.39	0.56	0.37	0.42	0.33	0.42	0.52	0.45	0.15	0.11	0.14	0.23	0.27	0.22	0.11	0.13
Al_2O_3	1.96	2.01	2.50	2.61	2.52	2.19	2.54	2.74	2.15	2.20	2.04	1.81	1.90	1.91	1.92	1.94	1.97	1.92	1.78	1.93	1.82	2.01
Cr_2O_3	0.19	0.20	0.39	0.50	0.38	0.30	0.32	0.50	0.27	0.21	0.10	0.08	0.20	0.09	0.38	0.39	0.43	0.24	0.29	0.30	0.55	0.23
FeO	6.75	6.13	4.89	4.51	4.78	5.05	4.78	4.79	5.15	5.55	5.77	6.06	5.92	5.84	9.20	9.40	9.27	11.10	11.57	11.39	8.96	11.71
MnO	0.39	0.36	0.14	0.10	0.10	0.14	0.12	0.11	0.13	0.14	0.17	0.18	0.19	0.17	0.19	0.19	0.19	0.23	0.25	0.24	0.19	0.23
MgO	15.76	16.28	16.48	15.75	15.95	16.61	16.27	15.77	16.20	16.30	16.38	16.24	16.04	16.11	32.04	31.89	32.33	30.35	29.71	29.93	32.14	30.32
CaO	22.23	22.26	23.15	23.62	23.30	23.07	23.32	22.76	23.36	22.66	22.65	22.61	22.41	23.07	0.80	0.72	0.67	0.90	1.15	0.95	0.73	0.74
Na_2O	0.40	0.43	0.27	0.25	0.25	0.30	0.24	0.31	0.28	0.30	0.26	0.28	0.32	0.28	0.01	0.02	0.02	<0.01	0.01	<0.01	0.01	0.01
K_2O	<0.01	<0.01	<0.01	<0.01	<0.01	<0.01	<0.01	<0.01	<0.01	<0.01	<0.01	<0.01	<0.01	<0.01	<0.01	<0.01	0.01	0.02	0.04	0.01	<0.01	<0.01
NiO	0.02	0.02	0.03	0.03	0.03	0.02	0.01	0.02	0.02	0.02	0.01	0.02	0.02	0.02	0.05	0.05	0.04	0.03	0.02	0.03	0.05	<0.01
Total	100.3	100.3	99.66	99.84	99.71	99.66	99.86	99.29	99.79	99.70	99.51	99.52	99.78	99.49	100.1	100.3	100.5	99.76	99.77	99.75	100.7	99.93
Structural formulae on the basis of 6(O)																						
Si	1.915	1.908	1.883	1.912	1.912	1.892	1.899	1.909	1.902	1.906	1.906	1.910	1.923	1.900	1.933	1.940	1.927	1.936	1.941	1.942	1.950	1.927
Ti	0.012	0.011	0.013	0.011	0.010	0.010	0.011	0.016	0.010	0.012	0.009	0.012	0.014	0.012	0.004	0.003	0.004	0.006	0.007	0.006	0.003	0.003
Al	0.085	0.087	0.108	0.113	0.109	0.094	0.110	0.119	0.093	0.095	0.089	0.079	0.082	0.083	0.079	0.080	0.081	0.080	0.074	0.081	0.074	0.084
Cr	0.005	0.006	0.011	0.015	0.011	0.009	0.009	0.015	0.008	0.006	0.003	0.002	0.006	0.003	0.010	0.011	0.012	0.007	0.008	0.008	0.015	0.006
Fe^{3+}	0.085	0.099	0.108	0.044	0.054	0.113	0.078	0.040	0.095	0.084	0.097	0.096	0.061	0.109	0.037	0.026	0.048	0.029	0.024	0.017	0.005	0.050
Fe^{2+}	0.122	0.088	0.042	0.094	0.093	0.042	0.069	0.108	0.063	0.086	0.081	0.090	0.121	0.071	0.232	0.248	0.222	0.299	0.320	0.321	0.255	0.296
Mn	0.012	0.011	0.004	0.003	0.003	0.004	0.004	0.004	0.004	0.004	0.005	0.006	0.006	0.005	0.006	0.006	0.006	0.007	0.008	0.007	0.006	0.007
Mg	0.862	0.887	0.901	0.862	0.873	0.908	0.888	0.868	0.886	0.892	0.898	0.892	0.880	0.885	1.669	1.659	1.676	1.601	1.572	1.582	1.664	1.597
Ca	0.874	0.872	0.910	0.929	0.917	0.906	0.915	0.900	0.918	0.892	0.893	0.893	0.883	0.911	0.030	0.027	0.025	0.034	0.044	0.036	0.027	0.028
Na	0.028	0.031	0.019	0.017	0.018	0.021	0.017	0.022	0.020	0.022	0.019	0.020	0.023	0.020	0.000	0.001	0.001	0.000	0.001	0.000	0.000	0.001
K	0.000	0.000	0.000	0.000	0.000	0.000	0.000	0.000	0.000	0.000	0.000	0.000	0.000	0.000	0.000	0.000	0.000	0.001	0.002	0.001	0.000	0.000
Quadrilateral endmembers (mol %)																						
En	46	48	49	46	46	49	47	46	47	48	48	48	47	47	86	86	87	83	81	82	86	83
Fs	7	5	2	5	5	2	4	6	3	5	4	5	6	4	12	13	12	15	17	17	13	15
Wo	47	47	49	49	49	49	49	48	49	48	48	48	47	49	2	1	1	2	2	2	1	1

Table 3. Microprobe analyses of plagioclase in the olivine gabbro of the Khamal mafic intrusion.

Sample No.	**KG7**										**KG12**									
Spot No.	**Pl#1**	**Pl#2**	**Pl#3**	**Pl#4**	**Pl#5**	**Pl#6**	**Pl#7**	**Pl#8**	**Pl#9**	**Pl#10**	**Pl#1**	**Pl#2**	**Pl#3**	**Pl#4**	**Pl#5**	**Pl#6**	**Pl#7**	**Pl#8**	**Pl#9**	**Pl#10**
SiO_2	45.42	45.57	45.84	49.81	45.88	45.53	50.29	45.60	46.08	49.69	48.97	45.98	50.21	48.26	45.55	49.14	47.78	45.71	48.32	49.77
TiO_2	0.02	0.03	0.02	0.03	0.04	0.04	0.00	0.02	0.04	0.01	0.18	0.03	0.00	0.03	0.02	0.01	0.17	0.02	0.02	0.02
Al_2O_3	34.99	35.05	34.94	31.96	34.82	34.90	31.43	34.90	34.68	31.54	32.04	34.64	31.59	33.22	34.92	32.44	32.47	34.87	33.34	31.99
Cr_2O_3	0.31	0.30	0.34	0.25	0.30	0.28	0.12	0.32	0.31	0.06	0.00	0.29	0.09	0.13	0.30	0.15	0.03	0.30	0.08	0.16
MnO	<0.01	0.01	0.01	<0.01	0.01	0.01	0.01	0.01	0.02	0.01	<0.01	0.02	<0.01	0.01	0.01	0.01	0.01	0.01	<0.01	0.01
MgO	0.02	0.02	0.03	0.02	0.02	0.02	0.01	0.02	0.03	0.02	0.02	0.01	0.02	0.01	0.02	0.01	0.02	0.02	0.02	0.01
CaO	18.76	18.07	17.66	15.60	17.58	17.75	15.46	18.15	17.52	16.07	16.55	17.35	15.74	16.20	18.34	16.68	17.29	17.90	16.64	16.08
Na_2O	1.43	1.50	1.60	2.29	1.68	1.60	2.46	1.53	1.75	2.33	2.10	1.73	2.64	2.07	1.50	1.87	2.13	1.58	2.17	2.10
K_2O	0.02	0.02	0.02	0.01	0.02	0.02	<0.01	0.02	0.02	<0.01	0.01	0.02	0.01	<0.01	0.02	0.01	0.01	0.02	<0.01	0.02
Total	100.95	100.57	100.45	99.95	100.36	100.14	99.78	100.56	100.44	99.71	99.87	100.07	100.29	99.92	100.68	100.31	99.90	100.42	100.59	100.15
Structural formula on the basis of 8(O)																				
Si	2.082	2.092	2.104	2.273	2.108	2.097	2.296	2.094	2.115	2.275	2.243	2.116	2.285	2.209	2.091	2.240	2.198	2.100	2.201	2.268
Ti	0.001	0.001	0.001	0.001	0.001	0.001	0.000	0.001	0.001	0.000	0.006	0.001	0.000	0.001	0.001	0.000	0.006	0.001	0.001	0.001
Al	1.890	1.896	1.890	1.719	1.885	1.895	1.691	1.889	1.876	1.702	1.730	1.879	1.694	1.792	1.889	1.743	1.761	1.888	1.790	1.718
Fe(ii)	0.012	0.012	0.013	0.010	0.012	0.011	0.005	0.012	0.012	0.002	0.000	0.011	0.003	0.005	0.012	0.006	0.001	0.012	0.003	0.006
Mn	0.000	0.000	0.000	0.000	0.000	0.000	0.000	0.000	0.001	0.000	0.000	0.001	0.000	0.000	0.000	0.000	0.000	0.000	0.000	0.000
Mg	0.001	0.001	0.002	0.001	0.001	0.001	0.001	0.001	0.002	0.001	0.001	0.001	0.001	0.001	0.001	0.001	0.001	0.001	0.001	0.001
Ca	0.921	0.889	0.869	0.763	0.865	0.876	0.756	0.893	0.861	0.788	0.812	0.856	0.767	0.794	0.902	0.815	0.852	0.881	0.812	0.785
Na	0.127	0.134	0.142	0.203	0.150	0.143	0.218	0.136	0.156	0.207	0.186	0.154	0.233	0.184	0.134	0.165	0.190	0.141	0.192	0.186
K	0.001	0.001	0.001	0.001	0.001	0.001	0.000	0.001	0.001	0.000	0.001	0.001	0.001	0.000	0.001	0.001	0.001	0.001	0.000	0.001
Endmembers (mol %)																				
Or	0.11	0.11	0.12	0.06	0.12	0.12	0.00	0.11	0.11	0.00	0.06	0.12	0.06	0.00	0.11	0.06	0.06	0.11	0.00	0.12
Ab	12.11	13.04	14.07	20.97	14.73	14.01	22.36	13.22	15.29	20.78	18.66	15.27	23.27	18.78	12.88	16.85	18.22	13.76	19.09	19.09
An	87.78	86.84	85.82	78.97	85.16	85.88	77.64	86.67	84.60	79.22	81.28	84.62	76.67	81.22	87.01	83.09	81.73	86.13	80.91	80.79

Table 4. Microprobe analyses of ilmenite rims around loveringite in the olivine gabbro of the Khamal mafic intrusion.

Sample No.	**KG7**										**KG12**								
Spot No	**Il#1**	**Il#2**	**Il#3**	**Il#4**	**Il#5**	**Il#6**	**Il#7**	**Il#8**	**Il#9**	**Il#10**	**Il#1**	**Il#2**	**Il#3**	**Il#4**	**Il#5**	**Il#6**	**Il#7**	**Il#8**	**Il#9**
SiO_2	0.17	0.01	0.01	0.01	0.02	1.02	0.03	1.84	0.01	0.01	0.01	0.01	0.00	<0.01	0.36	0.30	0.02	0.16	0.01
TiO_2	47.12	46.78	47.69	46.55	46.98	47.40	49.62	47.51	49.01	49.26	49.88	48.54	45.17	48.97	48.28	50.59	47.90	49.36	47.75
Al_2O_3	0.05	0.04	0.04	0.03	0.03	0.18	0.04	0.65	<0.01	0.02	0.04	0.01	0.04	0.02	0.12	0.05	0.05	0.01	0.05
Cr_2O_3	0.04	0.02	0.03	0.03	0.03	0.03	0.02	0.00	0.01	0.02	0.02	0.03	0.03	0.03	0.02	0.02	0.01	0.04	0.03
FeO	46.57	48.70	48.02	48.67	48.46	45.78	46.10	44.17	45.92	46.92	45.84	48.06	50.58	46.89	47.02	44.30	48.42	44.75	48.67
MnO	2.64	2.88	2.62	3.21	3.37	3.33	3.59	3.55	3.98	2.83	3.52	2.68	2.81	3.50	2.70	3.86	2.62	3.73	2.66
MgO	0.53	0.27	0.31	0.27	0.25	0.25	0.21	0.23	0.22	0.29	0.24	0.32	0.27	0.23	0.45	0.22	0.34	0.30	0.29
NiO	0.01	0.01	0.01	0.02	0.02	0.02	0.03	0.05	0.02	0.03	0.02	0.01	0.02	<0.01	0.01	0.01	0.05	0.03	0.03
CaO	0.07	0.05	0.03	0.10	0.19	1.19	0.11	1.88	0.43	0.12	0.12	0.03	0.05	0.04	0.49	0.47	0.01	0.58	0.03
Na_2O	0.11	0.02	0.03	0.01	0.01	<0.01	0.01	<0.01	<0.01	0.01	<0.01	0.02	<0.01	0.02	<0.01	0.01	<0.01	0.15	<0.01
P_2O_5	0.01	<0.01	<0.01	0.01	<0.01	0.01	<0.01	<0.01	<0.01	<0.01	<0.01	<0.01	0.01	<0.01	<0.01	0.01	<0.01	<0.01	0.01
Total	97.32	98.78	98.79	98.88	99.36	99.21	99.78	99.87	99.60	99.52	99.69	99.69	98.98	99.71	99.43	99.83	99.43	99.11	99.53
Structure formula on the basis of 3 (O)																			
Si	0.004	0.000	0.000	0.000	0.000	0.026	0.001	0.046	0.000	0.000	0.000	0.000	0.000	0.000	0.009	0.007	0.001	0.004	0.000
Ti	0.911	0.892	0.910	0.886	0.890	0.895	0.939	0.886	0.928	0.934	0.945	0.918	0.858	0.927	0.912	0.956	0.908	0.939	0.904
Al	0.002	0.001	0.001	0.001	0.001	0.005	0.001	0.019	0.000	0.001	0.001	0.000	0.001	0.001	0.004	0.001	0.002	0.000	0.001
Fe^{+3}	0.165	0.214	0.177	0.225	0.217	0.153	0.118	0.117	0.143	0.129	0.108	0.162	0.282	0.144	0.154	0.070	0.181	0.110	0.188
Fe^{+2}	0.836	0.819	0.841	0.805	0.804	0.808	0.853	0.799	0.824	0.860	0.858	0.849	0.786	0.843	0.834	0.861	0.840	0.836	0.836
Mn	0.057	0.062	0.056	0.069	0.072	0.071	0.077	0.074	0.085	0.061	0.075	0.057	0.060	0.075	0.057	0.082	0.056	0.080	0.057
Mg	0.020	0.010	0.012	0.010	0.009	0.009	0.008	0.009	0.008	0.011	0.009	0.012	0.010	0.009	0.017	0.008	0.013	0.011	0.011
Ca	0.002	0.001	0.001	0.003	0.005	0.032	0.003	0.050	0.012	0.003	0.003	0.001	0.001	0.001	0.013	0.013	0.000	0.016	0.001
Na	0.006	0.001	0.002	0.000	0.000	0.000	0.001	0.000	0.000	0.000	0.000	0.001	0.000	0.001	0.000	0.000	0.000	0.007	0.000
Cr	0.001	0.000	0.001	0.001	0.001	0.001	0.000	0.000	0.000	0.000	0.000	0.000	0.001	0.001	0.000	0.000	0.000	0.001	0.001
Ni	0.000	0.000	0.000	0.000	0.000	0.000	0.001	0.001	0.000	0.001	0.000	0.000	0.000	0.000	0.000	0.000	0.001	0.001	0.001
Endmembers (mol %)																			
Ilm ($FeTiO_3$)	84.1	82.1	84.4	80.9	81.1	84.4	85.6	85.9	83.6	86.4	86.2	85.0	78.9	84.4	84.9	87.5	84.1	85.4	83.8
Hm (Fe_2O_3)	8.3	10.7	8.9	11.3	10.9	7.7	5.9	5.9	7.2	6.5	5.4	8.1	14.1	7.2	7.7	3.5	9.1	5.5	9.4
Pyro ($MnTiO_3$)	5.7	6.2	5.6	6.9	7.2	7.1	7.7	7.4	8.5	6.1	7.5	5.7	6.0	7.5	5.7	8.2	5.6	8.0	5.7
Gk ($MgTiO_3$)	2.0	1.0	1.2	1.0	0.9	0.9	0.8	0.9	0.8	1.1	0.9	1.2	1.0	0.9	1.7	0.8	1.3	1.1	1.1

Table 5. Microprobe analyses of green spinel in the olivine gabbro of the Khamal mafic intrusion.

Sample No	**KG7**								**KG12**								
Spot No	**Spl #1**	**Spl #2**	**Spl #3**	**Spl #4**	**Spl #5**	**Spl #6**	**Spl #7**	**Spl #8**	**Spl #1**	**Spl #2**	**Spl #3**	**Spl #4**	**Spl #5**	**Spl #6**	**Spl#7**	**Spl #8**	**Spl #9**
SiO_2	0.05	0.06	0.01	0.06	0.01	0.09	0.01	0.06	0.06	<0.01	0.08	0.06	0.10	0.07	0.01	0.05	0.05
TiO_2	0.02	0.01	0.23	0.03	0.22	0.02	0.34	0.02	0.02	0.27	0.02	0.02	0.02	0.02	0.25	0.01	0.02
Al_2O_3	56.22	56.15	56.56	55.34	58.11	56.34	55.72	56.27	56.11	57.32	56.71	57.42	57.05	55.25	53.89	57.35	55.02
Cr_2O_3	1.43	0.95	1.35	2.05	1.57	1.00	1.58	2.21	0.85	2.18	1.24	1.14	0.65	1.95	2.66	1.31	2.00
FeO*	26.41	26.40	29.57	26.49	28.67	26.46	29.61	26.49	27.48	28.00	26.34	26.28	26.18	26.63	31.95	26.53	27.55
MnO	0.38	0.39	0.33	0.38	0.27	0.40	0.31	0.40	0.38	0.29	0.38	0.37	0.37	0.38	0.37	0.40	0.40
MgO	14.60	13.99	10.89	13.86	10.60	13.68	11.95	13.20	14.07	11.28	13.70	13.64	13.69	14.07	10.95	13.32	13.47
NiO	0.15	0.16	0.16	0.17	0.17	0.18	0.19	0.17	0.18	0.15	0.14	0.20	0.12	0.19	0.15	0.14	0.18
CaO	0.01	0.01	0.01	0.01	<0.01	0.06	0.07	0.02	0.01	<0.01	0.04	0.01	0.06	0.01	<0.01	<0.01	0.02
Na_2O	0.07	0.09	0.01	0.07	<0.01	0.07	0.02	0.09	0.07	0.05	0.06	0.07	0.06	0.08	0.01	0.08	0.09
K_2O	<0.01	<0.01	<0.01	0.03	<0.01	<0.01	<0.01	<0.01	<0.01	<0.01	<0.01	<0.01	<0.01	<0.01	<0.01	<0.01	<0.01
Total	99.34	98.20	99.11	98.47	99.62	98.30	99.78	98.90	99.24	99.54	98.71	99.22	98.30	98.65	100.23	99.18	98.79
Structural formulae on the basis of 4(O)																	
Ti	0.000	0.000	0.005	0.001	0.004	0.000	0.007	0.000	0.000	0.005	0.000	0.000	0.000	0.000	0.005	0.000	0.000
Al	1.780	1.799	1.830	1.777	1.867	1.807	1.789	1.803	1.783	1.841	1.811	1.823	1.826	1.770	1.744	1.825	1.768
Cr	0.030	0.020	0.029	0.044	0.034	0.022	0.034	0.047	0.018	0.047	0.026	0.024	0.014	0.042	0.058	0.028	0.043
Fe3+	0.189	0.180	0.131	0.178	0.090	0.170	0.164	0.149	0.198	0.101	0.162	0.152	0.159	0.188	0.188	0.147	0.188
Fe2+	0.404	0.421	0.548	0.425	0.564	0.432	0.511	0.453	0.422	0.537	0.435	0.440	0.435	0.418	0.545	0.452	0.440
Mn	0.009	0.009	0.008	0.009	0.006	0.009	0.007	0.009	0.009	0.007	0.009	0.008	0.009	0.009	0.009	0.009	0.009
Ni	0.003	0.004	0.004	0.004	0.004	0.004	0.004	0.004	0.004	0.003	0.003	0.004	0.003	0.004	0.003	0.003	0.004
Mg	0.585	0.567	0.446	0.563	0.431	0.555	0.485	0.535	0.566	0.458	0.554	0.548	0.554	0.570	0.448	0.536	0.547
End-members (mol %)																	
Spinel	58	57	45	56	43	56	49	53	57	46	55	55	55	57	45	54	55
Hercynite	29	32	46	31	49	34	40	35	31	45	34	35	35	30	41	36	32
Galaxite	1	1	1	1	1	1	1	1	1	1	1	1	1	1	1	1	1
Magnetite	9	9	7	9	5	9	8	7	10	5	8	8	8	9	9	7	9
Chromite	2	1	1	2	2	1	2	2	1	2	1	1	1	2	3	1	2
Ulvöspinel	0	0	0	0	0	0	1	0	0	1	0	0	0	0	1	0	0

Table 6. Microprobe analyses of loveringite in the olivine gabbro of the Khamal mafic intrusion.

Sample No.	KG7											KG12									
Spot No.	**LV-1**	**LV-2**	**LV-3 ***	**LV-3 ****	**LV-4**	**LV-5**	**LV-6 ***	**LV-6 ****	**LV-4**	**LV-6**	**LV-10**	**LV-1**	**LV-2 ***	**LV-2 ****	**LV-3**	**LV-4**	**LV-5**	**LV-6 ***	**LV-6 ****	**LV-7**	**LV-8**
SiO_2	0.19	0.09	0.10	0.11	0.08	0.19	0.11	0.31	0.17	0.02	0.11	0.22	0.06	0.10	0.08	0.10	0.22	0.09	0.11	0.21	0.18
TiO_2	60.11	59.02	63.04	57.46	59.96	60.79	63.07	58.17	59.33	56.20	59.63	59.80	61.03	56.10	58.15	60.88	60.63	62.22	58.34	58.54	60.01
Al_2O_3	0.98	0.92	1.50	0.83	0.98	1.04	1.52	0.91	1.03	0.84	0.98	1.06	1.52	0.87	0.93	1.02	1.06	1.47	1.16	1.07	1.22
Cr_2O_3	8.79	7.12	7.84	5.38	2.80	8.27	7.78	6.44	4.41	6.61	4.71	6.31	7.82	6.97	9.42	4.54	8.28	7.65	6.38	6.12	4.98
FeO*	16.82	17.33	12.61	20.26	21.02	16.33	13.22	20.79	19.21	20.37	19.25	18.56	15.47	19.23	15.22	18.62	16.36	14.33	19.85	18.16	18.02
MnO	0.14	0.16	0.24	0.15	0.14	0.13	0.27	0.14	0.15	0.12	0.14	0.11	0.23	0.12	0.21	0.13	0.12	0.23	0.13	0.09	0.09
MgO	1.13	1.80	2.09	0.75	1.03	1.48	2.31	0.88	1.08	0.81	1.06	1.44	1.81	0.74	2.04	1.32	1.48	2.14	0.97	1.38	1.09
CaO	3.03	2.76	3.49	1.74	2.57	3.07	3.56	2.62	2.76	2.05	2.56	2.59	3.36	1.85	2.35	2.64	3.09	3.28	2.26	1.80	2.42
NiO	0.05	0.06	0.03	0.02	0.07	0.05	0.04	0.06	0.06	0.06	0.06	0.04	0.03	0.08	0.04	0.06	0.04	0.05	0.01	0.07	0.03
ZnO	0.05	0.06	0.02	0.02	0.04	0.02	0.04	0.05	0.07	0.01	0.07	0.02	0.03	0.03	0.01	0.10	0.02	0.04	0.03	0.09	0.08
ZrO_2	3.84	4.78	3.56	4.89	4.15	3.77	3.62	4.11	3.65	4.62	4.38	3.99	3.53	5.12	4.56	4.05	3.81	3.49	4.66	4.74	4.37
V_2O_3	1.56	2.03	1.28	1.83	2.12	1.62	1.12	1.67	1.97	2.41	2.14	1.68	1.22	2.32	1.91	1.61	1.59	1.09	1.52	1.50	1.87
La_2O_3	0.76	0.92	0.01	2.24	1.02	0.73	0.00	0.74	0.88	1.49	0.96	1.07	0.03	1.80	1.54	0.98	0.72	0.01	1.39	1.98	1.80
Ce_2O_3	1.02	0.45	1.20	2.55	0.88	0.98	1.07	1.23	1.03	2.07	1.58	1.64	1.68	2.15	1.71	1.33	1.01	1.32	1.99	2.49	2.65
Nd_2O_3	0.20	0.09	0.02	0.21	0.21	0.18	0.03	0.15	0.12	0.37	0.11	0.15	0.05	0.33	0.28	0.18	0.18	0.04	0.17	0.27	0.25
Y_2O_3	0.19	0.29	0.13	0.25	0.21	0.14	0.14	0.29	0.15	0.32	0.17	0.14	0.15	0.27	0.15	0.14	0.21	0.16	0.20	0.25	0.24
UO_2	0.07	0.15	0.21	0.15	0.28	0.03	0.15	0.16	0.20	0.14	0.22	0.11	0.13	0.17	0.16	0.26	0.07	0.18	0.06	0.11	0.12
ThO_2	0.16	0.24	0.01	0.11	0.34	0.18	0.01	0.33	0.25	0.22	0.28	0.13	0.01	0.31	0.25	0.33	0.26	0.02	0.16	0.15	0.14
HfO_2	0.04	0.21	0.06	0.28	0.11	0.02	0.05	0.17	0.12	0.27	0.16	0.24	0.08	0.20	0.22	0.16	0.02	0.06	0.22	0.09	0.06
Total	99.13	98.46	97.42	99.22	98.00	99.01	98.11	99.19	96.63	98.99	98.55	99.31	98.24	98.75	99.24	98.45	99.19	97.86	99.62	99.11	99.61
Structural Formulae on the basis of 38(O)																					
A site																					
Ca	0.902	0.828	1.052	0.54	0.799	0.913	1.062	0.79	0.861	0.628	0.788	0.781	1.008	0.57	0.701	0.812	0.92	0.983	0.686	0.553	0.749
La	0.078	0.095	0.001	0.239	0.109	0.075	0	0.077	0.095	0.157	0.102	0.111	0.003	0.191	0.158	0.104	0.074	0.001	0.145	0.209	0.143
Ce	0.104	0.046	0.124	0.27	0.094	0.1	0.109	0.127	0.11	0.217	0.166	0.169	0.172	0.226	0.174	0.14	0.103	0.135	0.206	0.261	0.227
Nd	0.02	0.009	0.002	0.022	0.022	0.018	0.003	0.015	0.012	0.038	0.011	0.015	0.005	0.034	0.028	0.018	0.018	0.004	0.017	0.028	0.026
Y	0.028	0.043	0.019	0.039	0.032	0.021	0.021	0.043	0.023	0.049	0.026	0.021	0.022	0.041	0.022	0.021	0.031	0.024	0.03	0.038	0.037
U	0.004	0.009	0.013	0.01	0.018	0.002	0.009	0.01	0.013	0.009	0.014	0.007	0.008	0.011	0.01	0.017	0.004	0.011	0.004	0.007	0.008
Th	0.01	0.015	0.001	0.007	0.022	0.011	0.001	0.021	0.017	0.014	0.018	0.008	0.001	0.02	0.016	0.022	0.016	0.001	0.01	0.01	0.009
Total A	1.145	1.046	1.212	1.127	1.097	1.139	1.205	1.083	1.131	1.112	1.126	1.112	1.22	1.094	1.109	1.134	1.166	1.159	1.098	1.106	1.199
M sites																					
Si	0.053	0.025	0.028	0.032	0.023	0.053	0.031	0.087	0.05	0.006	0.032	0.062	0.017	0.029	0.022	0.029	0.061	0.025	0.031	0.06	0.052
Ti	12.557	12.428	13.344	12.524	13.096	12.693	13.216	12.307	12.999	12.094	12.889	12.656	12.858	12.143	12.174	13.151	12.67	13.088	12.426	12.619	13.048
Zr	0.52	0.652	0.488	0.691	0.587	0.51	0.492	0.564	0.518	0.644	0.614	0.547	0.482	0.718	0.619	0.567	0.516	0.476	0.643	0.662	0.616
Hf	0.003	0.016	0.005	0.022	0.009	0.002	0.004	0.013	0.009	0.021	0.012	0.018	0.006	0.016	0.017	0.012	0.002	0.005	0.017	0.007	0.005
Al	0.215	0.204	0.334	0.19	0.225	0.228	0.335	0.202	0.237	0.19	0.223	0.236	0.337	0.198	0.205	0.232	0.233	0.325	0.26	0.242	0.279
Cr	2.877	2.349	2.6	1.837	0.958	2.705	2.554	2.135	1.514	2.228	1.595	2.092	2.581	2.363	3.089	1.536	2.711	2.521	2.129	2.067	1.696
V	0.347	0.456	0.289	0.425	0.493	0.36	0.25	0.377	0.46	0.553	0.493	0.379	0.274	0.535	0.426	0.371	0.354	0.244	0.345	0.345	0.433
Fe(iii)	1.746	2.416	0.448	2.151	2.361	1.674	0.814	2.856	2.077	2.767	1.974	2.156	1.424	2.35	1.966	1.716	1.608	1.216	2.408	1.869	1.285
Mg	0.468	0.751	0.877	0.324	0.446	0.612	0.959	0.369	0.469	0.345	0.454	0.604	0.756	0.317	0.846	0.565	0.613	0.892	0.409	0.589	0.47
Mn	0.033	0.038	0.057	0.037	0.034	0.031	0.064	0.033	0.037	0.029	0.034	0.026	0.055	0.029	0.049	0.032	0.028	0.054	0.031	0.022	0.022
Fe(ii)	2.16	1.64	2.519	2.758	2.742	2.117	2.265	2.034	2.602	2.106	2.652	2.21	2.199	2.277	1.576	2.755	2.193	2.134	2.292	2.483	3.071
Ni	0.011	0.014	0.007	0.005	0.016	0.011	0.009	0.014	0.014	0.014	0.014	0.009	0.007	0.019	0.009	0.014	0.009	0.011	0.002	0.016	0.007
Zn	0.01	0.012	0.004	0.004	0.009	0.004	0.008	0.01	0.015	0.002	0.015	0.004	0.006	0.006	0.002	0.021	0.004	0.008	0.006	0.019	0.017
Total M	21	21	21	21	21	21	21	21	21	21	21	21	21	21	21	21	21	21	21	21	21

* Cores; ** Rims.

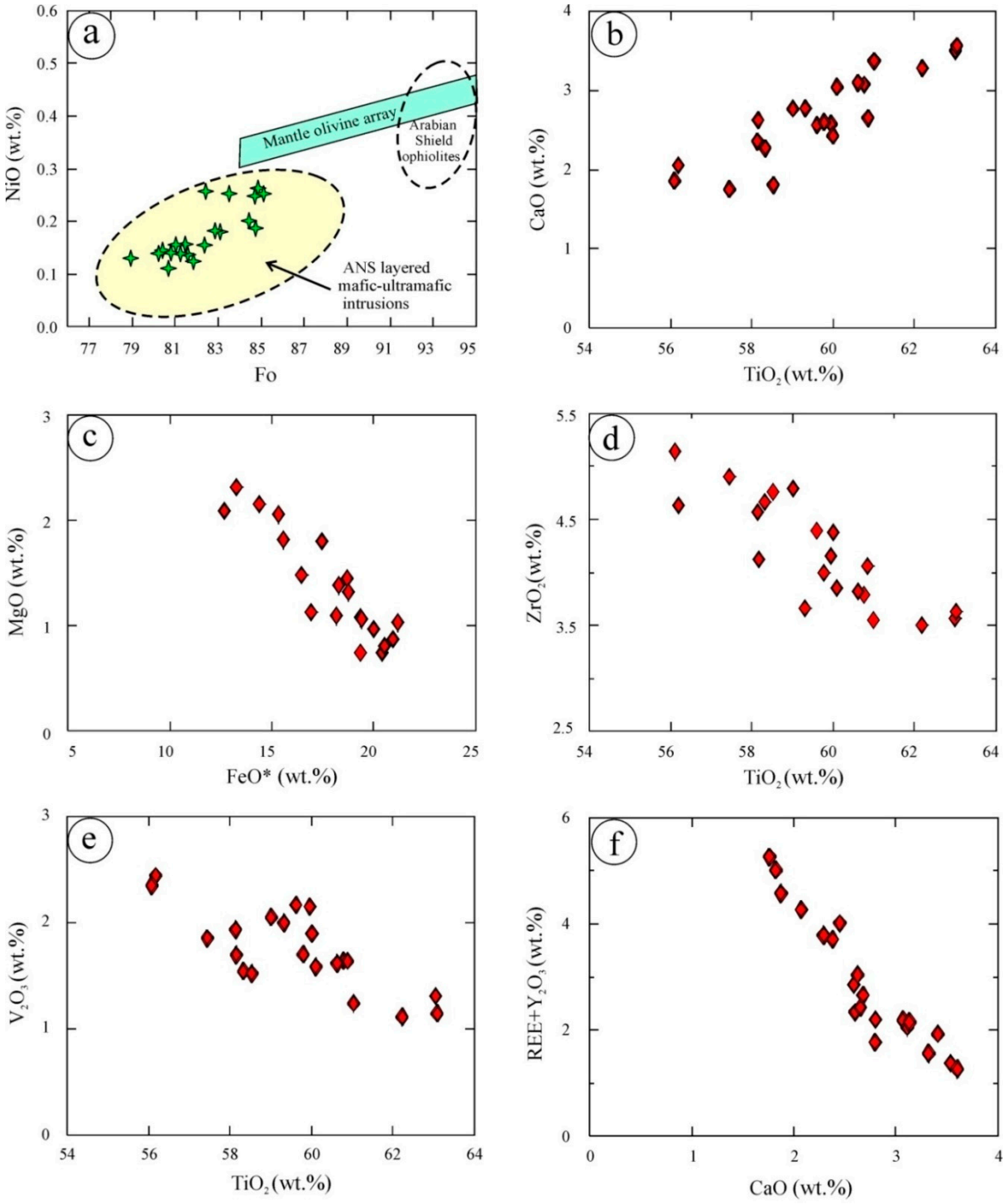

Figure 4. Mineral chemistry of the olivine gabbro: (**a**) variation of NiO (wt.%) and Fo contents of olivine in the olivine gabbro compared to the mantle olivine array [27], ANS layered intrusions [19,21,22]; and Arabian Shield ophiolites [13,23–26], (**b**–**f**) loveringite composition: (**b**) TiO_2 vs. CaO, (**c**) FeO* vs. MgO, (**d**) TiO_2 vs. ZrO_2, (**e**) TiO_2 vs. V_2O_3, and (**f**) CaO vs. REE + Y_2O_3.

4.6. Loveringite (Table 6)

Loveringite was found and analyzed in two samples (KG7 and KG12) of olivine gabbro from the Khamal mafic intrusion. The major oxides of Khamal loveringite are TiO_2 (56.1–63.1 wt.%), FeO^* (12.3–21.0 wt.%), Cr_2O_3 (2.8–9.4 wt.%), ZrO_2 (3.5–5.1 wt.%), CaO (1.7–3.6 wt.%), V_2O_3 (1.1–2.4 wt.%), Al_2O_3 (0.83–1.5 wt.%), and MgO (0.75–2.1 wt.%). Minor amounts of MnO, UO_2, ThO_2, light REE, Y_2O_3, HfO_2, NiO, and ZnO are also present. Structural formulae, following the original crystallographic reference [2], are normalized to 38 oxygen atoms. Large cations (Ca, La, Ce, Nd, Y, U, and Th) are placed on the A site and small cations (Si, Ti, Zr, Hf, Al, Cr, V, Fe^{3+}, Mg, Mn, Fe^{2+}, Ni, and Zn) are placed on the M site. The fraction of total Fe atoms that are Fe^{3+} is then obtained by assuming 21 occupied M sites per formula unit. This exercise yields an average formula of $(Ca_{0.81}La_{0.10}Ce_{0.16}Nd_{0.02}Y_{0.03}Th_{0.01}U_{0.01})_{\Sigma A=1.13}(Ti_{12.7}Fe^{3+}{}_{1.87}Fe^{2+}{}_{2.32}Cr_{2.20}Mg_{0.58}Al_{0.24}Si_{0.04}Zr_{0.58}Hf_{0.01}V_{0.39}Mn_{0.04}Ni_{0.01}Zn_{0.01})_{\Sigma M=21}O_{38}$, which can be simplified to $(Ca_{0.81}REE_{0.28}(Y,Th,U)_{0.05})_{\Sigma A=1.13}(Ti_{12.7}Fe^{3+}{}_{1.87}Fe^{2+}{}_{2.32}Cr_{2.20}Mg_{0.58}Al_{0.24}Zr_{0.58}V_{0.39}Mn_{0.04})_{\Sigma M=21}O_{38}$. This formula is remarkably consistent with the formula obtained by Gatehouse et al. [2] on the type specimen, which has 1.1 A cations per formula unit and is reported as $(Ca_{0.72}REE_{0.33}(Y,Th,U,Pb)_{0.05})_{\Sigma A=1.1}(Ti_{12.48}Fe^{*}{}_{3.38}Cr_{2.24}Mg_{0.92}Al_{0.39}Zr_{0.58}V_{0.21}Mn_{0.04})_{\Sigma M=20.34}O_{38}$ without correction for Fe^{3+}. Since the original discovery, a number of other loveringite localities around the world has been published, and their compositions are all similar to the new Khamal loveringite occurrence [4–8,33]. For example, the average composition from the Koitelainen intrusion (Finland) [5] is $(Ca_{0.51–0.82}La_{0.51–0.82}Ce_{0.14–0.28}U_{0.00–0.92})_{\Sigma A=0.99–1.08}(Ti_{12.25–13.04}Fe^{*}{}_{4.23–5.18}Cr_{1.18–1.94}Mg_{0.19–0.71}Al_{0.28–0.48}Si_{0.02–0.10}Zr_{0.54–0.75}Hf_{0.02}V_{0.11–0.22}Mn_{0.02–0.04})_{\Sigma M=20.02–20.92}O_{38}$. Most of the analyzed loveringite grains are homogeneous, except for a few zoned grains (see Table 6) with cores relatively richer in TiO_2, Al_2O_3, Cr_2O_3, MgO, and CaO and rims by contrast richer in FeO*, ZrO_2, V_2O_3, Y_2O_3, ThO_2, HfO_2, and REE. There is a positive correlation between TiO_2 and CaO (Figure 4b). On other hand, there are negative correlations between FeO* and MgO (Figure 4c), TiO_2 and ZrO_2 (Figure 4d), TiO_2 and V_2O_3 (Figure 4e), and CaO against REE + Y_2O_3 (Figure 4f). Some of these correlations may be understood directly from the crystal chemistry: Fe^{2+} and Mg compete to fill the M2 site, whereas Ca and REE + Y compete to fill the A site [2]. Other correlations, such as Ti vs. Zr and Ti vs. V, are less strictly governed by stoichiometry and suggest evolution during loveringite crystal growth in either the relative abundances of these cations in the intercumulus melt, in relative loveringite/melt partition coefficients, or both.

4.7. Baddeleyite (Table 7)

Six baddeleyite grains were analyzed. ZrO_2 is the major oxide and ranges between 91.9 and 93.5 wt.%, while other oxides (HfO_2, TiO_2, Al_2O_3, Cr_2O_3, FeO*, and MgO) occur in minor amounts. Some of the minor elements (Hf and Ti) can readily substitute for Zr in the baddeleyite structure; others likely represent errors due to secondary fluorescence from other minerals adjacent to the small analyzed baddeleyite crystals.

Table 7. Microprobe analyses of baddeleyite in the olivine gabbro of the Khamal mafic intrusion.

Sample No	KG7		KG12			
Spot No.	**Bd#1**	**Bd#2**	**Bd#3**	**Bd#4**	**Bd#5**	**Bd#6**
SiO_2	0.25	0.34	0.34	0.28	0.49	0.40
TiO_2	0.81	0.63	0.64	0.68	0.78	0.69
Al_2O_3	1.33	0.93	1.03	0.86	1.24	1.08
Cr_2O_3	1.57	1.28	1.24	0.98	1.12	1.24
FeO	1.49	1.11	1.27	1.36	1.36	1.31
MnO	0.05	0.05	0.05	0.06	0.03	0.04
MgO	0.68	0.73	0.78	0.58	0.61	0.69
CaO	0.03	0.05	0.04	0.05	0.03	0.04
NiO	0.05	0.07	0.07	0.08	0.07	0.06
ZrO_2	91.92	92.87	92.91	93.45	92.96	92.87
Ce_2O_3	0.08	0.12	0.07	0.07	0.05	0.08
Pr_2O_3	0.01	0.01	0.01	0.02	0.02	0.01
Nd_2O_3	0.01	0.01	0.02	0.01	0.03	0.02
Y_2O_3	0.01	0.04	0.03	0.03	0.02	0.02
ThO_2	0.02	0.02	0.02	0.03	0.01	0.02
HfO_2	0.94	1.07	1.02	0.98	0.87	0.96
Total	99.27	99.32	99.54	99.52	99.70	99.53

5. Discussion

To date, most occurrences of loveringite have been reported from layered intrusions [4,5,7,8,13,33]. The new occurrence is consistent with this, being found in the lowermost olivine gabbro unit of the Khamal layered intrusion, as anhedral to subhedral grains in interstices among intercumulus clinopyroxene and olivine grains, accompanied by apatite. This paragenesis is similar to those of loveringite in the Näränkavaara intrusion [33] and in the Monchepluton Layered Complex [14]. In the type locality, the Jimberlana Intrusion, there are rhythmically alternating layers of bronzite cumulate and olivine cumulate, overlain by a plagioclase + augite + hypersthene layer. In Jimberlana, loveringite is found in the bronzite cumulate layers and the lower half of the plagioclase + augite + hypersthene layer but is absent in the olivine cumulate layers [2].

In cumulate rocks, the whole-rock composition does not correspond to the parental liquid composition or to the liquid composition at any stage of magmatic evolution. Nevertheless, it is clear that the intercumulus liquid achieved saturation in several phases requiring significant enrichment in incompatible elements, namely loveringite, baddeleyite, and apatite. These phases are not early-crystallizing phases in typical mafic magmas, because REE, Zr, and P are generally not present in sufficient concentration. Although continued fractional crystallization of early mafic phases (olivine and pyroxenes) and plagioclase may drive the residual magma towards enrichment in these elements and saturation with such minor phases, this does not explain their presence in the basal layer of the Khamal intrusion. Instead, the paragenesis appears to require either (a) enrichment of the parental magma by assimilation of crustal contaminants, (b) isolation of the intercumulus liquid from the overlying magma, or most likely (c) both. In this scenario, the incompatible elements needed to crystallize loveringite, baddeleyite, and apatite would need to be present at some concentration in the magma already as the earliest-crystallized basal olivine gabbro layer is forming. Fractionation of mafic minerals would elevate concentrations of these elements in the local interstitial space, especially once crystallization of intercumulus phases reduces permeability and isolates the residual liquid. The incompatible elements would then not escape the basal layer, instead continuing to be enriched until the liquid reaches saturation with accessory phases. Although such enrichment in intercumulus liquid likely occurs in all mafic intrusions, loveringite remains a rare phase, found in only a few intrusions. This suggests that additional enrichment in Ti, Cr, REE, Zr, and V is necessary. Assuming such unusual elevations of minor elements are derived from crustal components, the contamination of the magma must have occurred at an early stage, consistent with a hot intrusion partially melting fusible components of its country rock, rather than by continuous assimilation coupled to later cooling of the magma. A study of the whole-rock

geochemistry of the Khamal intrusion would help to resolve whether the primitive magma was in fact enriched by crustal components.

The ilmenite rims around loveringite imply that the residual intercumulus liquid continued to evolve, passing out of the stability field of loveringite in favor of a reaction of loveringite plus liquid to form ilmenite and baddeleyite. This implies either low temperature favoring ilmenite below a peritectic reaction or depletion of the residual liquid by more compatible behavior of Ti, Ca, Al, Cr, and other essential elements of loveringite, compared to V, Fe, Mn, REE, and Zr. The latter explanation is consistent with the chemical evolution captured in selected zoned loveringite grains.

This scenario is consistent with observations including the inclusion of some euhedral loveringite crystals in intercumulus plagioclase and the inclusion of apatite in loveringite. It is also partly consistent with experimental results, which find that loveringite is stable at a pressure of 0.75 GPa across the temperature range 1000–1050 °C [34], although it seems unlikely that the Khamal intrusion was emplaced at lower-crustal depths, given its post-tectonic setting, lack of deformation, and upper crustal country rocks. However, there is evidence that loveringite may have a substantially larger stability field. It has been reported as inclusions in garnet from a kimberlite pipe [12] and in mantle xenoliths [11,35,36], both indicating higher pressure. Indeed, experimental studies of other members of the crichtonite mineral group show stability up to 11 GPa and 1500–1600 °C [37]. Experimental evidence for lower pressure stability is absent, but its occurrence in a number of shallowly emplaced and undeformed layered intrusions implies such an extension of the stability field.

6. Conclusions

Loveringite was observed for the first time in the Arabian Shield, from the Khamal mafic intrusion. This post-collisional layered mafic intrusion is neither metamorphosed nor deformed; it is tilted to expose a section through the layered sequence. The olivine gabbro at the base of the Khamal intrusion contains olivine with forsterite contents (79–85) similar to primitive members of several layered mafic intrusions in the ANS. Loveringite is found in the olivine gabbro as anhedral to subhedral corroded crystals surrounded by reaction rims of Mn-ilmenite and baddeleyite. Euhedral crystals may be found included in intercumulus plagioclase and loveringite may include apatite. Loveringite crystals are mostly homogeneous in composition, but a few grains are zoned from cores rich in TiO_2, Al_2O_3, Cr_2O_3, and CaO towards rims rich in FeO*, ZrO_2, V_2O_3, Y_2O_3, and REE. Loveringite is restricted to the lowermost stratigraphic level of the mafic intrusion, implying enrichment of the magma in incompatible elements at an early stage of evolution of the whole intrusion, leading to local saturation in incompatible-rich phases in the intercumulus liquid of the early stage cumulates. The continued thermal and compositional evolution of the intercumulus, captured in the zoned loveringite grains, eventually led to a peritectic reaction that left loveringite corroded and surrounded by Mn-bearing ilmenite and baddeleyite rims.

Author Contributions: B.A.A.: Methodology, Formal analyses, Investigation, Resources, Writing—review and editing; F.A.: Software, Investigation, Resources, Writing—review and editing, Resources, Project Administration, Funding Acquisition; M.K.A.: Conceptualization; Methodology, software, Formal analyses, Investigation, Validation; Data curation; Writing—original draft and revision, Visualization, Supervision; P.D.A.: Software, Investigation, Data curation, Writing—review and editing, Validation. All authors have read and agreed to the published version of the manuscript.

Funding: This research was funded by Abdullah Alrushaid Chair for Earth Science Remote Sensing Research at King Saud University, Riyadh, Saudi Arabia.

Data Availability Statement: The data presented in this study will be published with the manuscript.

Acknowledgments: The authors extend their appreciation to Abdullah Alrushaid Chair for Earth Science Remote Sensing Research for funding.

Conflicts of Interest: The authors declare no conflict of interest.

References

1. Campbell, I.H.; Kelly, P.R. The Geochemistry of Loveringite, a Uranium-Rare-Earth-Bearing Accessory Phase from the Jimberlana Intrusion of Western Australia. *Mineral. Mag.* **1978**, *42*, 187–193. [CrossRef]
2. Gatehouse, B.M.; Grey, G.I.; Campbell, I.H.; Kelly, P. The Crystal Structure of Loveringite, a New Member of the Crichtonite Group. *Am. Mineral.* **1978**, *63*, 28–36.
3. Cameron, E.N. An Unusual Titanium-Rich Oxide Mineral from the Eastern Bushveld Complex. *Am. Mineral.* **1978**, *63*, 37–39.
4. Mutanen, T. *Geology and Ore Petrology of the Akanvaara and Koitelainen Mafic Layered Intrusions and the Keivitsa-Satovaara Layered Complex, Northern Finland (Vol. 395)*; Geological Survey of Finland: Espoo, Finland, 1997.
5. Tarkian, M.; Mutanen, T. Loveringite from the Koitelainen Layered Intrusion, Northern Finland. *Mineral. Petrol.* **1987**, *37*, 37–50. [CrossRef]
6. Barkov, A.Y.; Pakhomovskii, Y.A.; Trofimov, N.N.; Lavrov, M.M. Loveringite: A First Occurrence in Russia, from the Burakovsky Layered Intrusion, Karelia. *Neues Jahrb. Für Mineral. Monatshefte* **1994**, *3*, 101–111.
7. Barkov, A.Y.; Saychenko, Y.E.; Men'shikov, Y.P.; Barkova, L.P. Loveringite from the Last-Yavr Mafic-Ultramafic Intrusion, Kola Peninsula; a Second Occurrence in Russia. *Nor. Geol. Tidsskr.* **1996**, *76*, 115–120.
8. Lorand, J.P.; Cottin, J.Y.; Parodi, J.C. Occurrence and Petrological Significance of Loveringite in the Western Laouni Layered Complex, Southern Hoggar, Algeria. *Can. Mineral.* **1987**, *25*, 683–693.
9. Stribrny, B.; Wellmer, F.-W.; Burgath, K.-P.; Oberthür, T.; Tarkian, M.; Pfeiffer, T. Unconventional PGE Occurrences and PGE Mineralization in the Great Dyke: Metallogenic and Economic Aspects. *Miner. Deposita* **2000**, *35*, 260–280. [CrossRef]
10. Cabella, R.; Gazzotti, M.; Lucchetti, G. Loveringite and Baddeleyite in Layers of Chromian Spinel from the Bracco Ophiolitic Unit, Northern Apennines, Italy. *Can. Mineral.* **1997**, *35*, 899–908.
11. Almeida, V.; Janasi, V.; Svisero, D.; Nannini, F. Mathiasite-Loveringite and Priderite in Mantle Xenoliths from the Alto Paranaíba Igneous Province, Brazil: Genesis and Constraints on Mantle Metasomatism. *Open Geosci.* **2014**, *6*, 614–632. [CrossRef]
12. Rezvukhin, D.I.; Malkovets, V.G.; Sharygin, I.S.; Tretiakova, I.G.; Griffin, W.L.; O'Reilly, S.Y. Inclusions of Crichtonite-Group Minerals in Cr-Pyropes from the Internatsionalnaya Kimberlite Pipe, Siberian Craton: Crystal Chemistry, Parageneses and Relationships to Mantle Metasomatism. *Lithos* **2018**, *308–309*, 181–195. [CrossRef]
13. Barkov, A.Y.; Sharkov, E.V.; Nikiforov, A.A.; Korolyuk, V.N.; Silyanov, S.A.; Lobastov, B.M. Compositional Variations of Apatite and REE-Bearing Minerals in Relation to Crystallization Trends in the Monchepluton Layered Complex (Kola Peninsula). *Russ. Geol. Geophys.* **2021**, *62*, 427–444. [CrossRef]
14. Harbi, H. Geology and Lithostratigraphy of the Ultramafic-Mafic Rocks and Associated Mineralizations, Wadi Khamal Area, West-Central Arabian Shield. *J. King Abdulaziz Univ.-Earth Sci.* **2008**, *19*, 119–157. [CrossRef]
15. Eldougdoug, A.; Abd El-Rahman, Y.; Harbi, H. The Ediacaran Post-Collisional Khamal Gabbro-Anorthosite Complex from the Arabian Shield and Its Fe-Ti-P Ore: An Analogy to Proterozoic Massif-Type Anorthosites. *Lithos* **2020**, *372–373*, 105674. [CrossRef]
16. Gahlan, H.A.; Azer, M.K.; Al-Hashim, M.H.; Osman, M.S. New insights and constraints on the late Neoproterozoic post-collisional mafic magmatism in the Arabian Shield, Saudi Arabia. *Lithos* **2022**, *436–437*, 106989. [CrossRef]
17. Pallister, J.S.; Stacey, J.S.; Fischer, L.B.; Premo, W.R. Precambrian Ophiolites of Arabia: Geologic Settings, U-Pb Geochronology, Pb-Isotope Characteristics, and Implications for Continental Accretion. *Precambrian Res.* **1988**, *38*, 1–54. [CrossRef]
18. Stern, R.J.; Johnson, P. Continental Lithosphere of the Arabian Plate: A Geologic, Petrologic, and Geophysical Synthesis. *Earth-Sci. Rev.* **2010**, *101*, 29–67. [CrossRef]
19. Essawy, M.A.; El-Metwally, A.A.; Althaus, E. Pan-African Layered Ultramafic- Mafic Cumulate Complex in the SW Sinai Massif: Mineralogy, Geochemistry and Crustal Growth. *Chem. Erde* **1977**, *57*, 137–156.
20. Azer, M.K.; El-Gharbawy, R.I. The Neoproterozoic Layered Mafic–Ultramafic Intrusion of Gabal Imleih, South Sinai, Egypt: Implications of Post-Collisional Magmatism in the North Arabian–Nubian Shield. *J. Afr. Earth Sci.* **2011**, *60*, 253–272. [CrossRef]
21. Abdel Halim, A.H.; Helmy, H.M.; Abd El-Rahman, Y.M.; Shibata, T.; El Mahallawi, M.M.; Yoshikawa, M.; Arai, S. Petrology of the Motaghairat Mafic–Ultramafic Complex, Eastern Desert, Egypt: A High-Mg Post-Collisional Extension-Related Layered Intrusion. *J. Asian Earth Sci.* **2016**, *116*, 164–180. [CrossRef]
22. Azer, M.K.; Gahlan, H.A.; Asimow, P.D.; Al-Kahtany, K.M. The Late Neoproterozoic Dahanib Mafic-Ultramafic Intrusion, South Eastern Desert, Egypt: Is It an Alaskan-Type or a Layered Intrusion? *Am. J. Sci.* **2017**, *317*, 901–940. [CrossRef]
23. Abuamarah, B.A.; Asimow, P.D.; Azer, M.K.; Ghrefat, H. Suprasubduction-Zone Origin of the Podiform Chromitites of the Bir Tuluhah Ophiolite, Saudi Arabia, during Neoproterozoic Assembly of the Arabian Shield. *Lithos* **2020**, *360–361*, 105439. [CrossRef]
24. Lasheen, E.S.R.; Saleh, G.M.; Khaleal, F.M.; Alwetaishi, M. Petrogenesis of Neoproterozoic Ultramafic Rocks, Wadi Ibib–Wadi Shani, South Eastern Desert, Egypt: Constraints from Whole Rock and Mineral Chemistry. *Appl. Sci. Switz.* **2021**, *11*, 10524. [CrossRef]
25. Gahlan, H.A.; Azer, M.K.; Asimow, P.D.; Hamimi, Z. The Mantle Section of Neoproterozoic Ophiolites from the Pan-African Belt, Eastern Desert, Egypt: Tectonomagmatic Evolution, Metamorphism, and Mineralization. In *The Geology of the Egyptian Nubian Shield*; Hamimi, Z., Arai, S., Fowler, A.-R., El-Bialy, M.Z., Eds.; Regional Geology Reviews; Springer International Publishing: Cham, Switzerland, 2021; pp. 309–341. ISBN 978-3-030-49770-5.
26. Gahlan, H.A.; Azer, M.K.; Asimow, P.D.; Al-Kahtany, K.M. Formation of Gold-Bearing Listvenite in the Mantle Section of the Neoproterozoic Bir Umq Ophiolite, Western Arabian Shield, Saudi Arabia. *J. Afr. Earth Sci.* **2022**, *190*, 104517. [CrossRef]

27. Takahashi, E.; Uto, K.; Schilling, J.G. *Primary Magma Compositions and Mg/Fe Ratios of Their Mantle Residues along Mid-Atlantic Ridge 29N to 73N*; Technical Report, A9, Institute of Studies Earth's Interior; Okayama University: Tottori-Ken, Japan, 1987.
28. Morimoto, N. Nomenclature of Pyroxenes. *Mineral. Petrol.* **1988**, *39*, 55–76. [CrossRef]
29. Störmer, J.C. The Effects of Recalculation on Estimates of Temperatures and Oxygen Fugacity from Analyses of Multicomponent Iron-Titanium Oxides. *Am. Mineral.* **1983**, *68*, 586–594.
30. Deer, W.A.; Howie, R.A.; Zussman, J. *An Introduction to the Rock Forming Minerals*, 2nd ed.; Longman Scientific and Technical: London, UK, 1992.
31. Abdel-Karim, A.-A.; Azer, M.K.; Sami, M. Petrogenesis and tectonic implications of the Maladob ring complex in the South Eastern Desert, Egypt: New insights from mineral chemistry and whole-rock geochemistry. *Int. J. Earth Sci.* **2020**, *110*, 53–80. [CrossRef]
32. Sami, M.; Ntaflos, T.; Mohamed, H.A.; Farahat, E.S.; Hauzenberger, C.; Mahdy, N.M.; Abdelfadil, K.M.; Fathy, D. Origin and Petrogenetic Implications of Spessartine Garnet in Highly-Fractionated Granite from the Central Eastern Desert of Egypt. *Acta Geol. Sin.-Engl. Ed.* **2020**, *94*, 763–776. [CrossRef]
33. Alapieti, T.T.; Filen, B.A.; Lahtinen, J.J.; Lavrov, M.M.; Smolkin, V.F.; Voitsekhovsky, S.N. Early Proterozoic Layered Intrusions in the Northeastern Part of the Fennoscandian Shield. *Mineral. Petrol.* **1990**, *42*, 1–22. [CrossRef]
34. Green, T.H.; Pearson, N.J. High-Pressure, Synthetic Loveringite-Davidite and Its Rare Earth Element Geochemistry. *Mineral. Mag.* **1987**, *51*, 145–149. [CrossRef]
35. Wang, L.; Essene, E.J.; Zhang, Y. Mineral Inclusions in Pyrope Crystals from Garnet Ridge, Arizona, USA: Implications for Processes in the Upper Mantle. *Contrib. Mineral. Petrol.* **1999**, *135*, 164–178. [CrossRef]
36. Kalfoun, F.; Ionov, D.; Merlet, C. HFSE Residence and Nb/Ta Ratios in Metasomatised, Rutile-Bearing Mantle Peridotites. *Earth Planet. Sci. Lett.* **2002**, *199*, 49–65. [CrossRef]
37. Konzett, J. Phase Relations and Stability of Magnetoplumbite- and Crichtonite-Series Phases under Upper-Mantle P-T Conditions: An Experimental Study to 15 GPa with Implications for LILE Metasomatism in the Lithospheric Mantle. *J. Petrol.* **2004**, *46*, 749–781. [CrossRef]